Ciliary control of meiotic chromosomal pairing mechanics and germ cell morphogenesis

Avishag Mytils[1,*], Vineet Kumar[1,*], Qiu Tao[2], Rachael Deis[1], Karine Levy[1], Markus Masek[3], Hagai Eitan[1], Farouq Nather[1], Amal Shawahny[1], Ruxandra Bachmann-Gagescu[3,4], Sudipto Roy[2,5,6], and Yaniv M. Elkouby[1,†].

***Equal contribution**

[1]Department of Developmental Biology and Cancer Research, The Hebrew University of Jerusalem Faculty of Medicine, Institute for Medical Research Israel-Canada (IMRIC), Ein-Kerem Campus, Jerusalem, 9112102, Israel. [2]Institute of Molecular and Cell Biology, Proteos, 61 Biopolis Drive, Singapore 138673 [3]Department of Molecular Life Sciences, University of Zurich, Winterthurerstrasse 190, 8057 Zurich, Switzerland [4]Institute of Medical Genetics, University of Zurich, Wagistrasse 12, 8952 Schlieren, Switzerland [5]Department of Biological Sciences, National University of Singapore, 14 Science Drive 4, Singapore 117543 [6]Department of Pediatrics, Yong Loo Lin School of Medicine, National University of Singapore, 1E Kent Ridge Road, Singapore 119288

[†] Corresponding author: yaniv.elkouby@mail.huji.ac.il

Abstract

Meiosis is a cellular program essential for the production of haploid gametes. A hallmark of meiosis is chromosomal pairing via synaptonemal complexes, and a major focus traditionally has been to understand synaptonemal complex formation. However, chromosomal pairing also depends on cytoplasmic counterparts that tether and rotate telomeres on the nuclear envelope, shuffling chromosomes and mechanically driving their homology searches[1-8]. Rotating telomeres slide on perinuclear microtubules and are ultimately pulled towards the centrosome[7,9,10], forming the "zygotene chromosomal bouquet configuration"[11]. The bouquet is universally conserved and is essential for pairing and fertility[1-8,12]. However, despite its discovery in 1900[11], how the cytoplasmic counterparts of bouquet formation are mechanically regulated has remained enigmatic. Here, by studying zebrafish oogenesis, we report and comprehensively characterize the "zygotene cilium" - a previously unrecognized cilium in oocytes. We show that the zygotene cilium specifically connects to the bouquet centrosome and constitutes a cable system of the cytoplasmic bouquet machinery. Farther, zygotene cilia extend throughout the germline cyst, a conserved cellular organization of germ cells. By analyzing multiple ciliary mutants, we demonstrate that the zygotene cilium is essential for chromosomal pairing, germ cell morphogenesis, ovarian development and fertility. We further show that the zygotene cilium is conserved in both male meiosis in zebrafish, as well as in mammalian oogenesis. Our work uncovers the novel concept of a cilium as a critical player in meiosis and sheds new light on reproduction phenotypes in ciliopathies. Furthermore, most cells in metazoans are ciliated and exhibit specific nuclear dynamics. We propose a cellular paradigm that cilia can control chromosomal dynamics.

Recent breakthroughs have dissected the structure of synaptonemal complexes and how synaptonemal complex proteins and meiosis-specific cohesins assemble to pair homologous chromosomes[13-20]. However, the nuclear events of meiosis occur in the cellular context of a differentiating gamete, where chromosomal pairing depends on cytoplasmic counterparts. In pairing, telomeres perform a unique function. At the leptotene stage, telomeres tether to Sun/Kash complexes on the nuclear envelope (NE), which associate with perinuclear microtubules (MTs) via dynein[1-8]. This facilitates telomere rotations around the NE during leptotene-zygotene stages, which in turn shuffle chromosomes, driving their search for homologs. The perinuclear MTs at these stages emanate from the centrosome MT organizing center (MTOC)[7,9,10]. Ultimately, rotating telomeres are pulled towards the centrosome and cluster on the centrosome side of the NE, while looping their chromosomes to the other side - a configuration called the zygotene chromosomal bouquet[11]. Telomere clustering stabilizes initial pairing between homologous chromosomes, and is essential for synapsis, homologous recombination, and fertility[1-8,12].

The bouquet configuration was discovered in 1900[11] and is conserved from yeast to mammals[1-8]. However, how the cytoplasmic counterparts of bouquet formation are mechanically regulated in rotating telomeres is unknown. It is unclear how rotation forces are generated, counterbalanced to allow movements, and then halted at the correct stage. The global cellular regulation of the bouquet movements is unknown.

Rapid chromosomal rotations imply substantial forces in bouquet formation

We previously characterized the nuclear and cytoplasmic components of the bouquet and its formation in zebrafish oogenesis[10,21]. To obtain a better temporal resolution of bouquet formation, we performed live time-lapse analysis of bouquet chromosomal rotation in cultured ovaries[21] (Fig. 1A). This analysis revealed rapid rotational movements specifically in zygotene oocytes, in contrast with control oogonia and somatic pre-granulosa follicle cell nuclei, which do not execute

meiotic chromosomal pairing (Fig. 1A, Supp. Fig. 1A, Supp. Video 1-2). These rapid rotational movements suggest the underlying action of substantial mechanical forces. Rotating telomeres then cluster, strictly juxtaposing the centrosome[9,10,22] . Live recording of the centrosome during bouquet chromosomal rotations showed that it vibrates in place, remaining fixed at the same position in the cytoplasm (Supp. Video 3). Thus, like in mice[9], telomeres rotate and are pulled by MTs toward the centrosome to cluster. These observations suggest that ***1)*** MTs and the centrosome are subjected to mechanical strain during rotations, and ***2)*** the centrosome is likely to be physically anchored.

A newly identified zygotene cilium

We detected elongated fiber-like structures of acetylated tubulin that emanated from the centrosome at bouquet stages[10]. To our knowledge, such structures, which are highly reminiscent of cilia, have not been described before in oocytes of any species. A cilium is a MT-based organelle, comprised of an axoneme with stereotypically organized acetylated microtubule doublets that grow from the mother centriole (basal body) and extend extracellularly[23,24]. We reasoned that a stage-specific cilium-like structure is an intriguing candidate regulator of bouquet mechanics.

Several lines of evidence demonstrated that the zygotene acetylated tubulin structures are cilia. ***1)*** The specific ciliary marker Arl13b[25,26] colocalized with the acetylated tubulin (AcTub)-positive structures (Fig. 1B, D). ***2)*** Tubulin glutamylation (GluTub), another post-translational MT modification of ciliary axonemes, showed similar structures (Fig. 1C), that co-localized with the AcTub signal (Fig. 1D). ***3)*** Transgenic Arl13b-GFP in zygotene oocytes confirmed consistent ciliary structures in live ovaries (Supp. Fig. 1B). ***4)*** Transmission electron microscopy (TEM) of

Figure 1

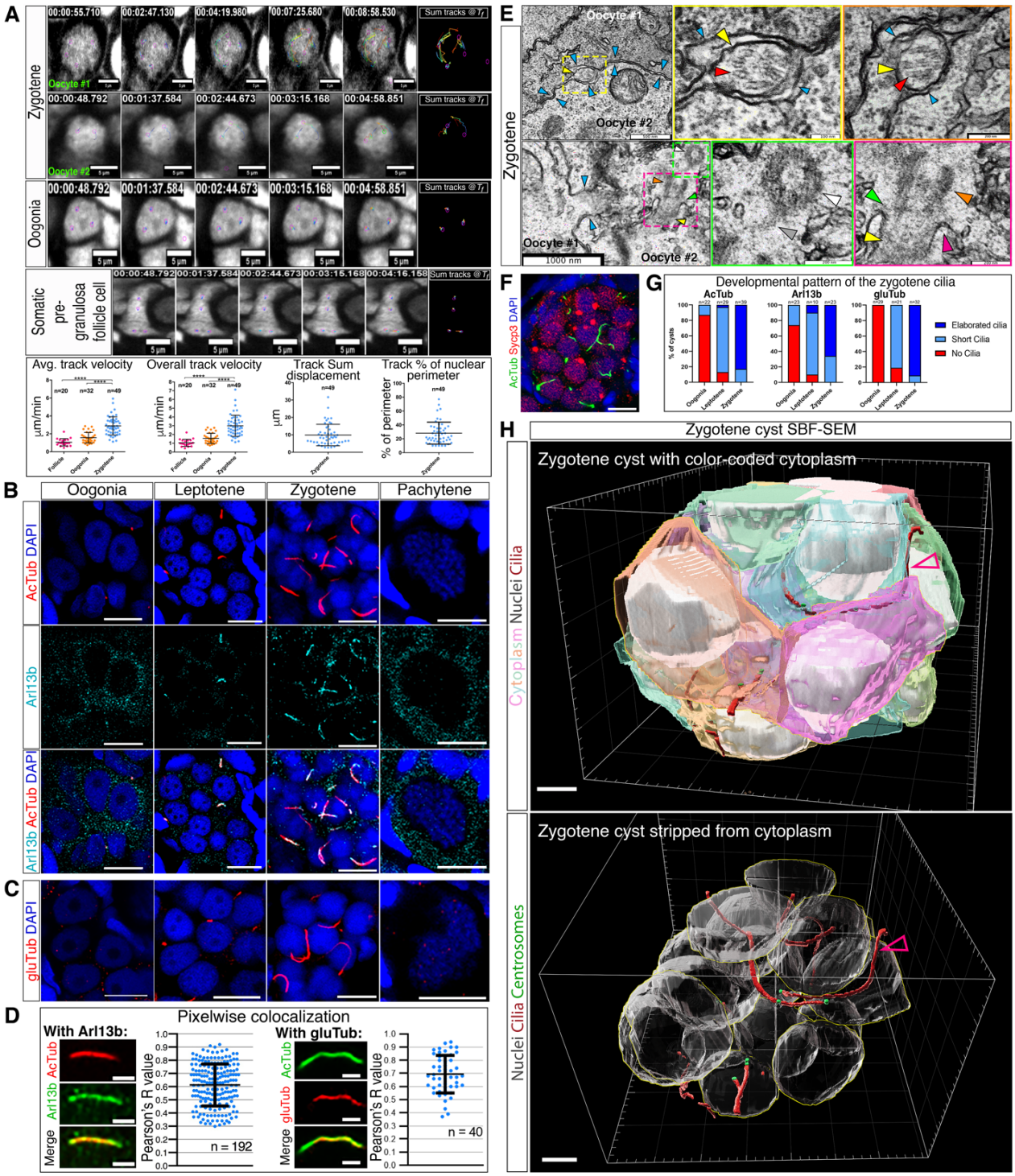

Figure 1. Bouquet chromosomal rotation dynamics and a zygotene specific oocyte cilium.

A. Live time-lapse imaging of *Tg(h2a:h2a-gfp)* (grey) ovaries, recording chromosomal dynamics of zygotene oocytes (two examples are shown), as well as oogonia and somatic pre-granulosa

follicle cells as controls. Sum of chromosomal tracks at T_f are shown for each cell. Images are snapshots from Supp. Video 1-2. Scale bars are 5 μm. n=34 zygotene oocytes, 17 oogonia, and 13 follicle cells, from 4 ovaries. Bottom panels are plots of average track velocity (point-to-point velocity), overall track velocity (sum displacement/track duration), track sum displacement, and % of track displacement relative to nuclear perimeter. n=number of tracks from representative cells. Cell averages are shown in Supp. Fig. 1A. **B.** AcTub and Arl13b labeling shown in oogonial, leptotene, and zygotene cysts, as well as pachytene oocytes. n=28 cysts in 8 ovaries. Scale bar for cyst panels is 5 μm and in pachytene panels 10 μm. **C.** GluTub labeling shown as in (A). n=82 cysts in 7 ovaries. Scale bars are as in (A). **D.** Pixelwise colocalization test and representative ROI images for AcTub and Arl13b, and for AcTub and gluTub. n=number of cilia. Bars are mean ± standard deviation (SD). **E.** TEM images of zygotene oocytes. Top panels: an axonemal structure, including ciliary membrane (yellow arrow) and MT doublets (red arrow) between cytoplasmic membranes of two oocytes (blue arrows). The two right panels are magnification of consecutive Z sections of the region boxed in the left panel. Bottom panels: ciliary structures within a zygotene oocyte, adjacent to a cytoplasmic bridge (blue arrows). Two right panels are magnification of the color-coded boxed regions in the left panel. In the three bottom panels, arrows indicate: centriole (white), linker (grey), basal body (orange) transition zone (green), ciliary pockets (pink), axoneme (yellow). Scale bars are indicated. **F.** AcTub and the prophase marker Sycp3 labeling shown in a zygotene cyst. n=24 cysts in 2 ovaries. Scale bar is 10 μm. **G.** The developmental distribution of the zygotene cilia as detected by AcTub (left; n>100 ovaries), Arl13b (middle; n=18 ovaries), and gluTub (right; n=11 ovaries). n=number of cysts. **H.** 3-D renders of a zygotene cyst SBF-SEM data, showing: cytoplasm of cyst oocytes (different transparent colors), nuclei (grey), cilia (maroon; maroon-grey arrowhead), and basal body centrosomes (green). Bottom panel: same cyst render stripped from cytoplasm to show the cilia. Scale bars are 5 μm.

ovaries identified structures that correspond to ciliary axonemes with typical MT doublets that are found in spaces between cell membranes of adjacent zygotene oocytes (Fig. 1E, top panels). Within oocytes, we identified the basal body, transition zone, and axoneme extending extracellularly through the ciliary pocket (Fig. 1E, bottom panels).

Cilia were present at the leptotene-zygotene stages as confirmed by the prophase synaptonemal complex marker Sycp3 (Fig. 1F). Interestingly, the cilia were stage-specific. They were absent from most pre-meiotic oogonial stages, but were detected as a few short cilia at leptotene, then fully elaborated at zygotene and were absent from the pachytene stage (Fig. B-C, G). This developmental pattern was consistently detected using either AcTub, Arl13b, or GluTub labeling (Fig. B-C, G). Based on these molecular, live imaging, and ultrastructural analyses, we conclude that we have been able to identify a previously unknown cilium in early prophase oocytes, specific to the zygotene stage.

Zygotene cilia extend throughout the germline cyst

Early prophase, including leptotene and zygotene stages, are executed while oocytes develop in the germline cyst[10,21,27], a conserved cellular organization of germ cells from insects to humans[28,29]. The germline cyst is generated during mitotic divisions of oocyte precursor cells called oogonia, whereby cytokinesis is incomplete, with cytoplasmic bridges (CBs) that persist between sister-cells and connect them[10,21,30,31]. In the cyst, germ cells are surrounded by somatic pre-granulosa cells[10,28,32]. The germline cyst is a compact and confined cellular organization, where cytoplasmic membranes of adjacent oocytes interface tightly[10].

The zygotene cilia extended throughout the volume of the cyst (Supp. Fig. 1C-D). To unequivocally characterize ciliary distribution in the cyst, we performed Serial Block-Face Scanning Electron Microscopy (SBF-SEM), providing ultrastructural data of cysts at EM resolution

in three-dimensions (3D; Methods; Supp. Video 4). Tracking the zygotene cilia in rendered leptotene and zygotene cysts in 3D (Fig. 1H, Supp. Video 4-5) confirmed that cilia tangle tightly between oocyte cytoplasmic membranes and extend throughout the cyst (Fig. 1J). Measurements of zygotene cilia diameters (Supp. Fig. 3A-B) showed the expected diameter of ciliary axonemes (~300nm[33]; Supp. Fig. 3A-B).

In the germline cyst, cytoplasmic bridges (CBs) are also based on MT cables[10,30]. Several lines of evidence allowed us to distinguish cilia and CBs in our analysis. ***1)*** In our TEM and SBF-SEM dataset, ciliary cytoplasm always showed axonemal MT tracks (Fig. 1E, Supp. Fig. 3B), but CB cytoplasm was indistinguishable from the remaining oocyte cytoplasm and often contained vesicles (Supp. Fig. 2A). CB membranes were typically ruffled and continuous with the cytoplasmic membranes of the connected oocytes (Supp. Fig. 2A). ***2)*** Measurements of CB diameters (Supp. Fig. 3), were consistent with those of CBs in *Xenopus* and mice (0.5-1 μm[34]), but not with the ciliary diameter. ***3)*** In contrast to cilia, CBs were adjacent to the centrosomes/basal bodies[10], but never associated with them. ***4)*** Cilia did not extend through, or co-localize with CBs as labeled by the midbody marker Cep55[35] (Supp. Fig. 2B, 3C-D). Thus, the zygotene cilia and CBs are distinct separate structures.

Our findings unravel a unique cytoskeletal arrangement of a cable system that extends from the zygotene cilium, through the centrosome and MT, to Sun/KASH-bound telomeres on the nuclear envelope, as the potential machinery for chromosomal pairing movements. Live time-lapse imaging confirmed that the zygotene cilium coincides with bouquet chromosomal rotations (Supp. Video 6). We next aimed to investigate the function of the zygotene cilium in oogenesis.

Loss of the zygotene cilium is associated with oogenesis failure and fertility deficiency

Severe disruption to ciliary differentiation causes embryonic lethality in zebrafish. However,

mutations in certain cilia genes allow viability to the adult stage. We analyzed multiple such *loss-of-function* ciliary mutants that in humans cause ciliopathies, genetic disorders that are caused by ciliary defects. These included Cep290 (*cep290*^{fh297} [36] and *cep290*^{fh378}*),* a basal body and transition zone protein that is required for cilia formation and transition zone assembly[37-42], Kif7 (*kif7*^{i271} [43]*)* an atypical kinesin that is required for organizing the ciliary tip compartment and for ciliary function and signaling through Shh[44-46], Cc2d2a (*cc2d2a*^{w38}), a transition zone protein and part of a multiprotein complex that acts as a gatekeeper to the ciliary compartment[47,48], and Armc9 (*armc9*^{zh505}), a ciliary base and tip protein that is required for ciliary stability and involved in hedgehog signaling[49-51].

We found that *cep290*$^{fh297/fh297}$*, cep290*$^{fh378/\ fh378}$*, cc2d2a*$^{w38/w38}$*,* and *armc9*$^{zh50/zh5055}$ adult females do not mate spontaneously (Supp. Fig. 4A), indicating defective oogenesis, or abnormal spawning or mating behavior that might be secondary to their characteristic cilia loss-scoliosis phenotype[36,47,50]. To test the abnormalities in oogenesis per se, we performed in vitro fertilization (IVF) assays. Most *cep290*$^{fh297/fh297}$*, cep290*$^{fh378/fh378}$*, cc2d2a*$^{w38/w38}$*,* and *armc9*$^{zh505/zh505}$ females produced degenerated eggs or no eggs at all (Supp. Fig. 4A-B). In line with their deficient fertility, *cep290*$^{fh297/fh297}$ and *cc2d2a*$^{w38/w38}$ females exhibited striking ovarian dysgenesis (Fig. 2A, Supp. Fig. 4C). In comparison to wt, mutant ovaries were smaller, underdeveloped, and exhibited degenerated masses of tissue (Fig. 2A, Supp. Fig. 4C). Pre-maturation (st. III) oocytes were mostly lacking or degenerated. These data suggest that cilia are required directly in oogenesis. We therefore examined developing gonads in these animals.

We analyzed the zygotene cilia in juvenile ovaries of *cep290*^{fh297} and *kif7*^{i271} mutants (hereafter referred to as *cep290*$^{-}$, and *kif7*$^{-}$*,* respectively), as well as *cc2d2a*$^{w38/w38}$ (below and Supp.Fig. 9). Based on wt ciliary length measurements in 3D (Fig. 2B, Supp. Fig. 5, Methods), we defined “normal cilia” (4-8.5 μm), “short cilia” (<4 μm), and absent cilia (N.D). Individual ciliary

Figure 2

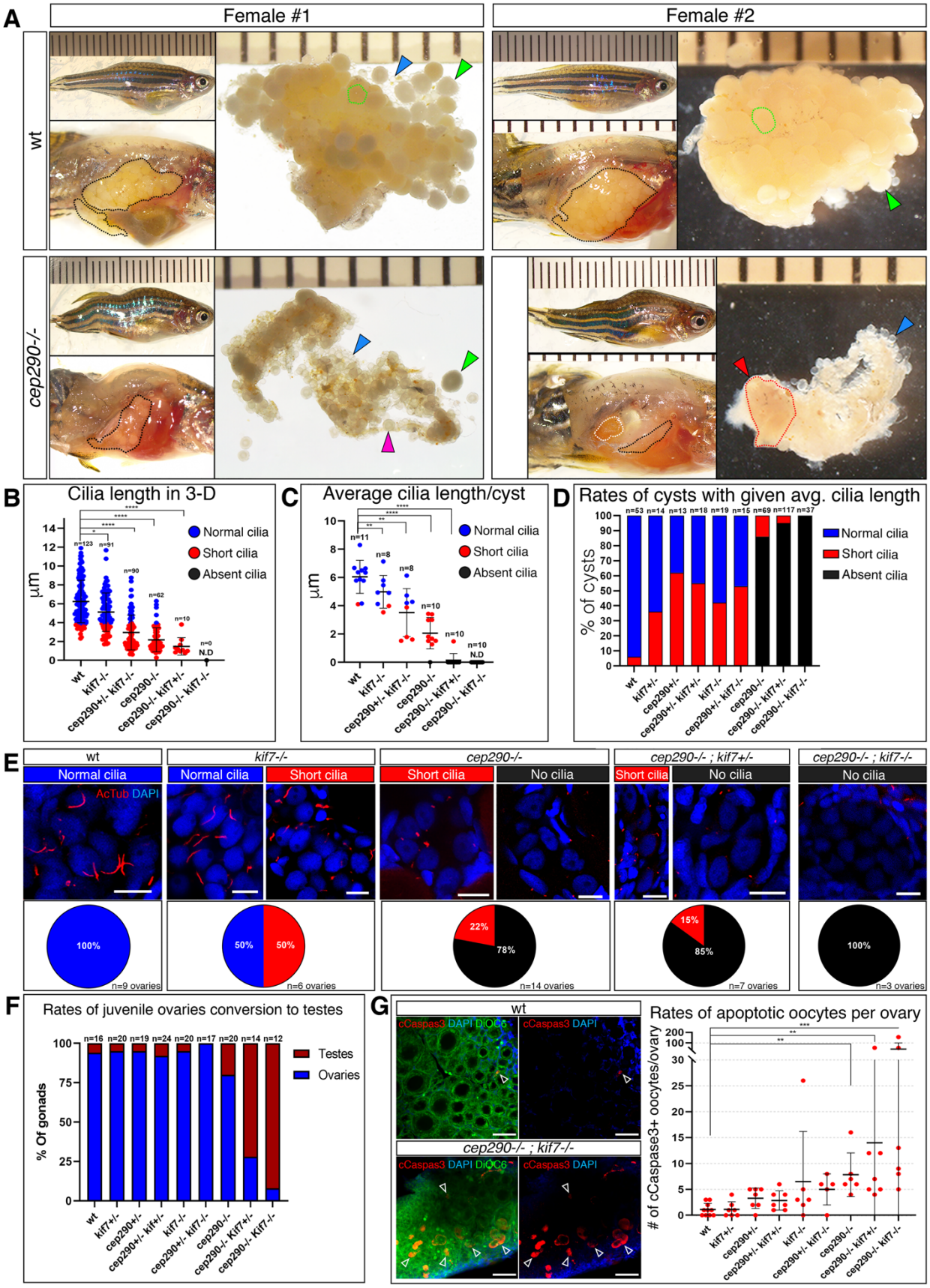
A
Female #1
Female #2
wt
cep290-/-
B
Cilia length in 3-D
µm
Normal cilia
Short cilia
Absent cilia
n=123
n=91
n=90
n=62
n=10
n=0
N.D
wt
kif7-/-
cep290+/- kif7-/-
cep290-/-
cep290-/- kif7+/-
cep290-/- kif7-/-
C
Average cilia length/cyst
µm
n=11
n=8
n=8
n=10
n=10
n=10
N.D
D
Rates of cysts with given avg. cilia length
% of cysts
n=53
n=14
n=13
n=18
n=19
n=15
n=69
n=117
n=37
E
wt
kif7-/-
cep290-/-
cep290-/- ; kif7+/-
cep290-/- ; kif7-/-
Normal cilia
Short cilia
No cilia
AcTub DAPI
100%
50%
50%
22%
78%
15%
85%
100%
n=9 ovaries
n=6 ovaries
n=14 ovaries
n=7 ovaries
n=3 ovaries
F
Rates of juvenile ovaries conversion to testes
% Of gonads
Testes
Ovaries
n=16
n=20
n=19
n=24
n=20
n=17
n=20
n=14
n=12
G
wt
cep290-/- ; kif7-/-
cCaspas3 DAPI DiOC6
cCaspas3 DAPI
Rates of apoptotic oocytes per ovary
# of cCaspase3+ oocytes/ovary

Figure 2. Loss of cilia, oocyte apoptosis, and ovarian dysgenesis in ciliary mutants. A. Wt (top panels) and *cep290*$^{-/-}$ (bottom panels) adult females and ovaries showing: ovaries within the peritoneal cavity (black outline), st.III premature oocytes (green arrows and outlines) that are scarce in *cep290*$^{-/-}$ ovaries, young transparent st.I oocytes (blue arrows), st.II oocytes (pink arrows), and degenerated tissue mass (red arrow and outline) as well as a completely degenerated ovary (white outline) in *cep290*$^{-/-}$ females. Ruler marks are 1 mm. *cep290*$^{-/-}$ females exhibit scoliosis, a typical ciliary phenotype. **B.** 3-D measurements of ciliary lengths. n=number of cilia. N.D, not detected. Bars are mean ± SD. **C.** Average ciliary length per cyst. n=number of cysts. Bars are mean ± SD. **D.** Distribution of cysts with normal and short ciliary length averages, as well as with absent cilia. **E.** Representative images (AcTub labeling) of cysts with indicated ciliary length categories as in B-D per genotype. Percentage of ovaries with indicated predominant categories are shown below. n=number of ovaries. Scale bars are 10 μm. **F.** Rates of juvenile gonad conversion per genotype. n=number of gonads. **G.** cCaspase3 apoptosis labeling (white arrows) in juvenile ovaries. Left panels: representative images of wt (top) and *cep290*$^{-/-}$*; kif7*$^{-/-}$ (bottom) ovaries. DiOC6 is a cytoplasmic marker. Scale bars are 50 μm. Right panel: number of cCaspase3-positive oocytes per gonad for all genotypes. Each dot represents a gonad, n=5-10 gonads per genotype. Bars are mean ± SD.

---

lengths (Fig. 2B), average ciliary length per cyst (Fig. 2C), distribution of scored cysts (Fig. 2D), and scoring of entire ovaries (Fig. 2E), established gradual loss of zygotene cilia in *cep290;kif7* mutant combinations. Ovaries of *kif7*$^{-/-}$, and heterozygote combinations showed mild partial phenotypes (Fig. 2B-E, Supp. Fig. 5), and *cep290*$^{-/-}$ ovaries showed either absent or short cilia. Attempting to abolish cilia altogether, we generated *cep290;kif7* double mutants. In *cep290*$^{-/-}$*; kif7*$^{+/-}$ and *cep290*$^{-/-}$*; kif7*$^{-/-}$ ovaries, cilia were mostly or completely abolished.

In juvenile *cep290*$^{-/-}$*; kif7*$^{+/-}$ and *cep290*$^{-/-}$*; kif7*$^{-/-}$ fish, most gonads converted to testes (Fig. 2D). In the zebrafish, gonads initially develop as ovaries that execute normal oogenesis[10,21]. Sex determination then dictates continuation of ovarian development or their conversion to testes[52-54], resulting in ~1:1 female:male ratio. Sex determination in laboratory zebrafish depends on environmental cues, and the mechanism is not completely understood[52-55]. However, the induction of oocyte loss by P53 dependent apoptosis results in conversion to testes[52,53]. Multiple oocyte defective mutants, including meiotic mutants, convert to testes and develop as sterile males[53,56], likely activating meiotic checkpoint-induced apoptosis similar to mouse oogenesis[57,58]. In wt and heterozygous mutants, we detected up to ~10% conversion (Fig. 2F), which represent occasional earlier sex determination. In contrast, 20% of *cep290*$^{-/-}$ ovaries, ~78% of *cep290*$^{-/-}$*;kif7*$^{+/-}$, and ~90% of *cep290*$^{-/-}$*;kif7*$^{-/-}$ ovaries were converted (Fig. 2F).

Gonad conversion strongly suggests early oocyte apoptosis[52,53,56]. In wt juvenile ovaries, apoptotic oocytes are rare[59], as detected by cleaved Caspase3 in wt, *cep290,* and *kif7* heterozygous combination fish (Fig. 2G). We detected more apoptotic oocytes in *cep290*$^{-/-}$*, kif7*$^{-/-}$, and *cep290*$^{+/-}$*; kif7*$^{-/-}$ ovaries, and this was significantly increased in *cep290*$^{-/-}$*; kif7*$^{+/-}$ and *cep290*$^{-/-}$*; kif7*$^{-/-}$ ovaries (Fig. 2G), where most gonads eventually converted to testes (Fig. 2F). Consistent with this, we observed a male bias in *cep290*$^{-/-}$ adults (Supp. Fig. 6). Most *cep290*$^{-/-}$*;kif7*$^{+/-}$ and *cep290*$^{-/-}$*;kif7*$^{-/-}$ animals do not survive to adulthood, precluding systematic adult analysis, but survivors consistently exhibited male bias as well (Supp. Fig. 6). These results confirm that without the zygotene cilium, early oocytes fail to develop, and instead undergo apoptosis, indicating severe defects.

The zygotene cilium is required for bouquet formation and chromosomal pairing

We examined bouquet formation in juvenile ovaries. In *cep290*$^{-/-}$ and *cep290*$^{-/-}$*;kif7*$^{-/-}$ ovaries, oocytes at zygotene stages were fewer or absent, suggesting that prophase progression is

defective. Wt leptotene and zygotene oocytes are 7-9 and 10-15 μm in diameter, respectively[10,21]. In mutants, we identified oversized "leptotene-like" oocytes, defined as oocytes with leptotene-like radial telomere distribution, which are larger than the largest detected wt leptotene oocyte (>9.1 μm; Fig. 3A-B). In heterozygous, *kif7*$^{-/-}$, and *cep290*$^{+/-}$; *kif7*$^{-/-}$ ovaries, ~40-65% of oocytes with radial telomeres were mildly larger leptotene-like oocytes (Fig. 3A-B, Supp. Fig. 7A). In *cep290*$^{-/-}$ ovaries, 85% were much larger leptotene-like oocytes (9-11 μm; Fig. 3A-B, Supp. Fig. 7A). This suggests that oocytes continue to grow in size, but bouquet formation is at least delayed.

cep290$^{-/-}$; *kif7*$^{-/-}$ and *cep290*$^{-/-}$; *kif7*$^{+/-}$ ovaries were severely affected, converted to testes (Fig. 2F) and contained low numbers of oocytes for analysis. Nevertheless, we captured double homozygous *cep290*$^{-/-}$;*kif7*$^{-/-}$ ovaries prior to or during conversion. In *cep290*$^{-/-}$;*kif7*$^{-/-}$, 100% of oocytes with radial telomeres were very large leptotene-like oocytes (10-12 μm; Fig. 3A-B, Supp. Fig. 7A), suggesting a greater delay. Oocytes with activated zygotene meiotic checkpoints in mice continue to grow and are cleared by apoptosis later at pachytene stages[57,58], suggesting that similar dynamics are likely for zebrafish "leptotene-like" oocytes.

We tested whether oocytes ultimately formed proper bouquet configuration. Telomere distribution in wt mid-bouquet stages (Fig. 3C, Methods) showed either tight telomere cluster, or a slightly expanded cluster ("Tight" and "Expanded" in Fig. 3C). Ovaries of heterozygous, *kif7*$^{-/-}$, and *cep290*$^{+/-}$; *kif7*$^{-/-}$ fish were mostly similar to wt. However, in *cep290*$^{-/-}$ ovaries, in addition to the wt categories, we detected an abnormal "dispersed" category (Fig. 3C), where telomeres were largely expanded beyond the nuclear equator (Fig. 3C). Moreover, in *cep290*$^{-/-}$; *kif7*$^{-/-}$ ovaries, we only detected "expanded" and "dispersed" category oocytes (Fig. 3C). Thus, with loss of functional cilia, telomeres do not cluster properly, remain distributed on the nuclear envelope, and fail to form the bouquet.

Figure 3

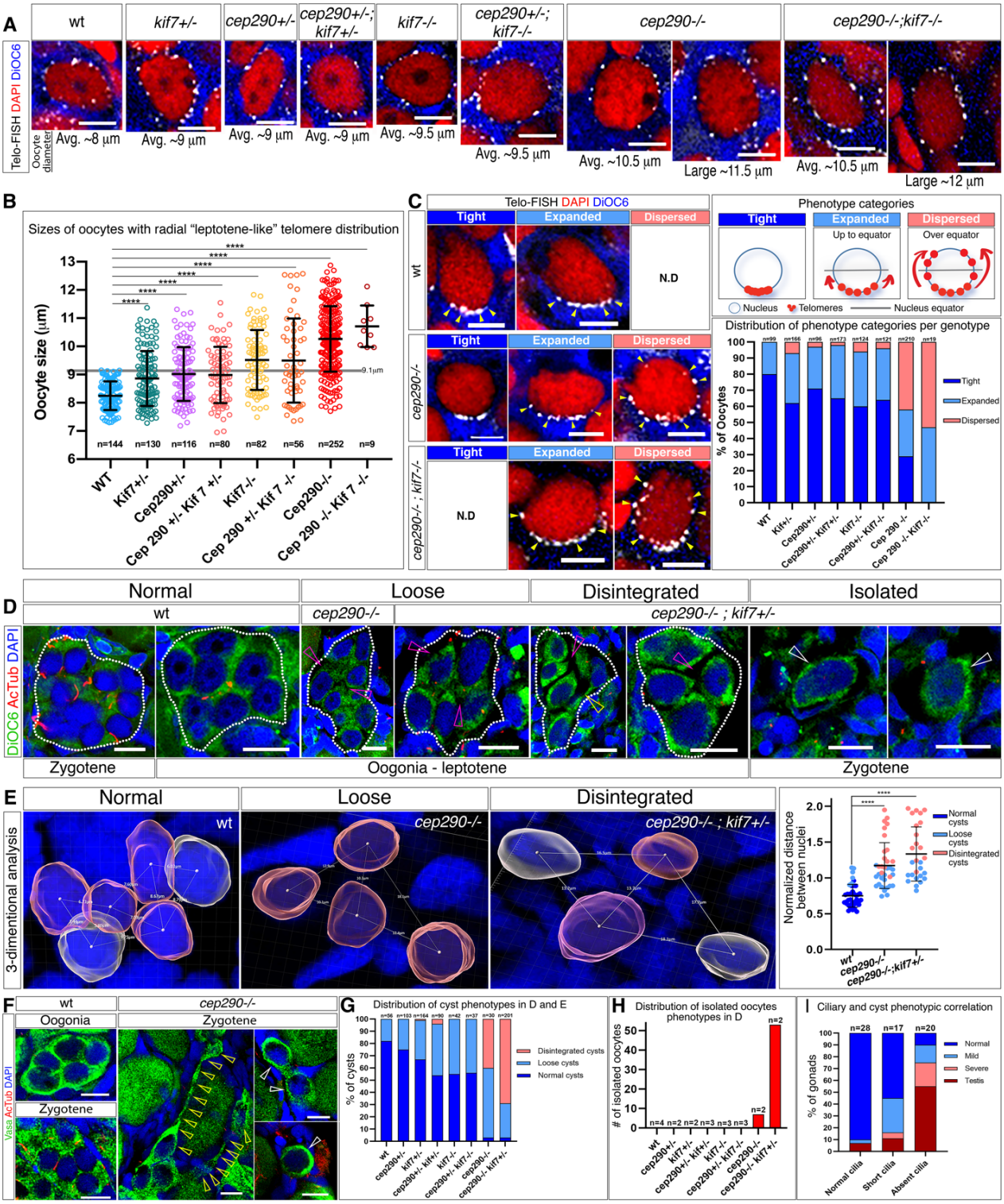
A
wt
kif7+/-
cep290+/-
cep290+/-; kif7+/-
kif7-/-
cep290+/-; kif7-/-
cep290-/-
cep290-/-;kif7-/-
Telo-FISH DAPI DiOC6
Oocyte diameter
Avg. ~8 µm
Avg. ~9 µm
Avg. ~9 µm
Avg. ~9 µm
Avg. ~9.5 µm
Avg. ~9.5 µm
Avg. ~10.5 µm
Large ~11.5 µm
Avg. ~10.5 µm
Large ~12 µm
B
Sizes of oocytes with radial "leptotene-like" telomere distribution
Oocyte size (µm)
9.1µm
n=144
n=130
n=116
n=80
n=82
n=56
n=252
n=9
WT
Kif7+/-
Cep290+/-
Cep 290 +/- Kif 7 +/-
Kif7-/-
Cep 290 +/- Kif 7 -/-
Cep290-/-
Cep 290 -/- Kif 7 -/-
C
Telo-FISH DAPI DiOC6
Tight
Expanded
Dispersed
wt
N.D
cep290-/-
cep290-/- ; kif7-/-
Phenotype categories
Up to equator
Over equator
Nucleus
Telomeres
Nucleus equator
Distribution of phenotype categories per genotype
% of Oocytes
Tight
Expanded
Dispersed
D
Normal
Loose
Disintegrated
Isolated
wt
cep290-/-
cep290-/- ; kif7+/-
DiOC6 AcTub DAPI
Zygotene
Oogonia - leptotene
Zygotene
E
Normal
Loose
Disintegrated
3-dimentional analysis
wt
cep290-/-
cep290-/- ; kif7+/-
Normalized distance between nuclei
Normal cysts
Loose cysts
Disintegrated cysts
F
wt
cep290-/-
Oogonia
Zygotene
Zygotene
Vasa AcTub DAPI
G
Distribution of cyst phenotypes in D and E
% of cysts
Disintegrated cysts
Loose cysts
Normal cysts
H
Distribution of isolated oocytes phenotypes in D
# of isolated oocytes
I
Ciliary and cyst phenotypic correlation
% of gonads
Normal
Mild
Severe
Testis
Normal cilia
Short cilia
Absent cilia

Figure 3. The zygotene cilium is required for bouquet formation and germline cyst morphogenesis. A. Representative images of "leptotene-like" oocytes of average sizes per genotype. Large "leptotene-like" *cep290*$^{-/-}$ and *cep290*$^{-/-}$*;kif7*$^{-/-}$ oocytes are shown. Scale bars are 5 μm. **B.** "Leptotene-like" oocyte sizes per genotype. n=number of oocytes. Bars are mean ± SD. 9.1 μm represents the largest wt leptotene oocytes. **C.** Left panel: representative images of mid-bouquet stage oocytes with Tight, Expanded, and Dispersed telomeres (categories shown in top right panel). N.D=non-detected. Scale bars are 5 μm. Right bottom panel: the percentage of each category in all genotypes. n=number of oocytes. **D.** Representative images of cyst (white outlines) phenotype categories in ovaries labeled for the cytoplasmic marker DiOC6 and AcTub, showing gaps between oocytes (magenta arrows), elongated cytoplasmic bridges (yellow arrows), and isolated oocytes (white arrows). Scale bars are 10 μm. The percentage of cyst phenotype categories and number of isolated oocytes in all genotypes from this experiment is shown in **G** (n=number of cysts) and **H** (n=number of ovaries). **E.** Representative images of 3-D cyst morphology analysis per category, showing the distances between neighboring nuclei. Normalized distances are plotted in the right panel. n=5-7 cysts from 2-3 ovaries per genotype. Bars are mean ± SD. **F.** Vasa and AcTub labeling shows normal cysts in wt ovaries, and disintegrated cysts (elongated CBs, yellow arrows), as well as isolated zygotene oocytes (white arrows) in *cep290*$^{-/-}$ ovaries. Phenotype distribution in all genotypes is plotted in Supp. Fig. 8**.** Scale bars are 10 μm. **I.** Severity of cyst phenotypes and gonad conversions plotted for three categories of ciliary defects pooled from all genotypes. n=number of gonads.

We determined whether these bouquet phenotypes arise directly due to ciliary defects. Cep290 subcellular localizations include the ciliary basal body and transition zone, as well as the centrosome and centriolar satellites[38,42,60-64]. Cep290 is essential for cilia biogenesis[37-42], but

whether it is required for centrosome MTOC functions in oocytes is unknown. In *cep290*$^{-/-}$ oogonia and early prophase oocytes, γTub recruitment to the centrosome, which is the final step in its MTOC maturation[65,66], was intact even in the most severe cases where cilia were completely absent (Supp. Fig. 7B). In line with this, MT perinuclear organization was not disrupted (Supp. Fig. 7C). This demonstrates that the centrosome MTOC functions are unaltered, confirming that the observed bouquet defects arise directly from the loss of cilia.

The zygotene cilium is required for germline cyst morphogenesis

We further found that the morphology of germline cysts in mutant ovaries was abnormal. Wt cysts are compact, with no gaps between cytoplasmic membranes of adjacent oocytes[10], as detected by DiOC6 cytoplasmic staining ("Normal" in Fig. 3D). However, we observed two abnormal cyst phenotype categories in *cep290*$^{-/-}$ and *cep290*$^{-/-}$*; kif7*$^{+/-}$ ovaries (Fig. 3D, G): "loose cysts" with abnormal gaps between oocytes, and more severe "disintegrated cysts" with larger gaps and exposed elongated cytoplasmic bridges (Methods section). To quantify cyst disintegration, we measured the distances between the centers of all neighboring nuclei in 3D in wt, *cep290*$^{-/-}$*,* and *cep290*$^{-/-}$*; kif7*$^{+/-}$ cysts (Fig. 3E; Supp. Video 7), normalized to the average oocyte diameter per cyst (Fig. 3E right panel). These measurements showed that the normalized distances between neighboring nuclei in *cep290*$^{-/-}$*,* and *cep290*$^{-/-}$*; kif7*$^{+/-}$ cysts were significantly increased compared to the wt (Fig. 3E).

Strikingly, we observed an additional category of "isolated oocytes" in *cep290*$^{-/-}$ and *cep290*$^{-/-}$*;kif7*$^{+/-}$ ovaries (Fig. 3D, H). Isolated oocytes are zygotene stage oocytes that are never seen outside the germline cyst in wt ovaries, but are found individually scattered in *cep290*$^{-/-}$ and *cep290*$^{-/-}$*;kif7*$^{+/-}$ ovaries (Fig. 3D), further indicating their disintegration from cysts. Overall, in contrast to wt, heterozygous, and *kif7*$^{-/-}$ ovaries*,* ovaries of *cep290*$^{-/-}$ and *cep290*$^{-/-}$*; kif7*$^{+/-}$ fish barely contained normal cysts, but instead mostly disintegrated cysts and isolated oocytes (Fig. 3G-H).

cep290$^{-/-}$*; kif7*$^{-/-}$ gonads converted to testes in these experiments, preventing oocyte analysis, but indicating that they were severely defective.

Labeling ovaries with the germ cell-specific marker Vasa confirmed the detection of disintegrated cysts where long cytoplasmic bridges extended between distant oocytes (Fig. 3F, Supp. Fig. 8A). These oocytes exhibited oval and irregular cellular morphology that coincides with their likely abnormal separation (Fig. 3F). Vasa labeling also detected isolated zygotene oocytes in doublets and singlets (Fig. 3F, Supp. Fig. 8B). Further, later pachytene and diplotene stage oocytes exhibited irregular mesenchymal-like cellular morphology in *cep290*$^{-/-}$ ovaries, instead of their smooth spherical morphology in the wt (Supp. Fig. 8C). Disintegration of cysts in our Vasa experiments was mostly apparent in *cep290*$^{-/-}$ mutants, while *cep290*$^{-/-}$*; kif7*$^{+/-}$ and *cep290*$^{-/-}$*; kif7*$^{-/-}$ were converted to testes (Supp. Fig. 8A). These results show that the zygotene cilium is required for cyst integrity and morphogenesis.

In all the experiments above we co-labeled cilia by AcTub staining and simultaneously analyzed cyst integrity and ciliary phenotypes. We performed correlation analysis between these phenotypes by categorizing gonads from all genotypes (n=43 gonads, 10-60 cysts were analyzed per gonad, see Methods) based on their ciliary phenotype (normal, short, absent, as in Fig. 2B-E), and separately their cyst integrity phenotypes (normal, mild, severe in Fig. 3). Cross-referencing these data revealed a strong correlation between the severity of ciliary loss and severity of cyst phenotypes (Fig. 3I), and is in line with our findings that ciliary defects directly underlie bouquet phenotypes (Supp. Fig. 7). Complete ciliary loss predicts conversion to testes, which represents oocyte loss and the most severe phenotype, in ~60% of gonads (Fig. 3I).

Finally, we detected consistent ciliary loss, and its associated bouquet perturbations, germline cyst disintegration, and conversion to testes in *cc2d2a*$^{-/-}$ juvenile gonads (Supp. Fig. 9), where we also found ovarian dysgenesis and fertility deficiencies in adults (Supp. Fig. 4). This further

independently demonstrates that the zygotene cilium is required for chromosomal pairing, germ cell morphogenesis, and ovarian development.

The zygotene cilium is conserved in male meiosis and mouse oogenesis

Considering the importance of zygotene cilia in oogenesis, we examined whether it also forms during spermatogenesis. In juvenile testes, co-labeling of AcTub with the cytoplasmic membrane marker β-catenin, and with the prophase marker Sycp3, detected cilia-like structures within developing seminiferous tubules, specifically in prophase spermatocytes (Supp. Fig. 10A).

Sperm flagella are specialized form of cilia that are composed of similar acetylated tubulin-positive axonemes[67]. Flagella formation begins after prophase, at mid-round spermatid stages, and completes by the mature spermatozoa stage[67]. We analyzed developed seminiferous tubules in adult testes, where all spermatogenesis stages can be detected, to distinguish potential zygotene cilia from flagella. We co-labeled AcTub with three prophase spermatocyte markers separately: telomere dynamics as visualized by Telo-FISH[22], Sycp3[56], and γH2Ax[56] (Fig. 4A-C). Round spermatids had AcTub-positive flagella (E2 in Fig. 4A-C; see staging criteria in the Methods section), and flagella of spermatozoa were very long and swayed within the lumen of the tubules (E3 in Fig. 4A-C). Strikingly, zygotene stage spermatocytes with the characteristic bouquet patterns of telomeres (Telo-FISH), Sycp3, and γH2Ax[22,56], showed clear AcTub-labeled cilia (Fig. 4A-C).

In pachytene spermatocytes and E1 early round spermatid stages, some showed AcTub-positive cilia while others did not (Fig. 4A, B), suggesting an intermediate time window during/between zygotene cilia removal and flagella formation. TEM analysis confirmed ciliary structures in zygotene spermatocytes (Fig. 4D), and these were distinct from flagella structures

Figure 4

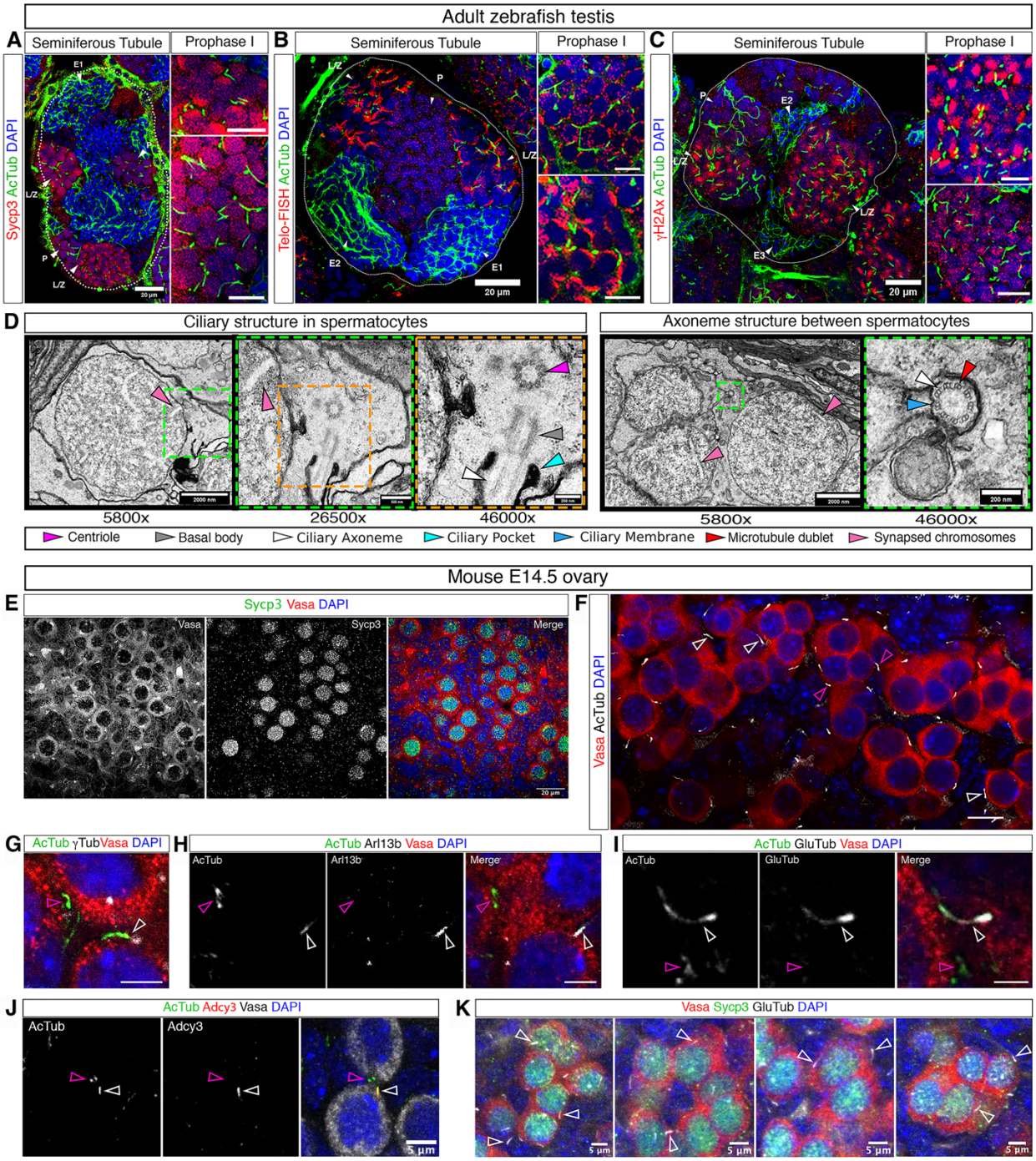

Figure 4. The zygotene cilium is conserved in zebrafish male meiosis and mouse oogenesis. A-C. Seminiferous tubules of adult zebrafish testes labeled with AcTub and Sycp3 (**A**, n=35 tubules in 3 testes) or Telo-FISH (**B**, n=29 tubules in 2 testes) or gH2Ax (**C**, n=34 tubules

in 3 testes). In **A-C**, left panels are optical sections of entire tubules (white outline, scale bars are 20 μm). The right panels are zoom-in images of prophase spermatocytes (scale bars are 10 μm). L/Z - Leptotene/Zygotene Primary Spermatocytes, P - Pachytene Spermatocytes, E1 - Initial Spermatids, E2 - Intermediate Spermatids, E3 - Final (Mature) Spermatids. **D.** TEM images of adult testis showing ciliary structures (as indicated by arrowheads and the legend) within (left panels) and between (right panels) prophase spermatocytes (identified by their synapsed chromosomes, pink arrowheads). Color-framed panels are larger magnification images of color-matched boxes in left panels. Magnifications and scale bars are as indicated. **E.** Mouse E14.5 ovaries labeled with Vasa and Sycp3. Scale bar is 20 μm. **F.** Mouse E14.5 ovaries labeled with Vasa and AcTub, showing AcTub-positive CBs (pink arrows) and cilia (white arrows) in Vasa labeled cysts. n=4 ovaries. Scale bar is 15 μm. **G-J.** E14.5 ovaries labeled with AcTub, Vasa, and γTub (**G**, n=2 ovaries), or Arl13b (**H**, n=2 ovaries), or GluTub (**I**, n=2 ovaries), or Adcy3 (**J**, n=2 ovaries). Scale bars are 5 μm. **K.** E14.5 ovaries co-labeled with Vasa, Sycp3, GluTub, and DAPI. Representative cyst images are shown, taken from larger frames, such as in Supp. Fig. 10 (n=2 ovaries). Scale bars are 5 μm. In E-J, cilia (white arrows), and CB-like structures (pink arrows) are indicated.

---

in the lumen of seminiferous tubules which exhibited clear central MT pair and radial spokes[67] (Supp. Fig. 10C). Thus, the zygotene cilium is a separate structure than the flagellum, and shows the same meiotic pattern in spermatogenesis as in oogenesis.

Bouquet mechanisms of meiotic chromosomal pairing are universal in sexually reproducing species [1-9,68-71]. Considering this, we examined whether the zygotene cilium is conserved in mammals. In the mouse fetal ovary, oocyte development is synchronized[72-75]. Sycp3 labeling showed that E14.5 ovaries contained mostly early prophase oocytes (Fig. 4E), as

expected[72-75]. AcTub labeling of E14.5 ovaries identified two structures in Vasa-positive germline cysts: one resembled a cytoplasmic bridge (CB), and the other a cilium (Fig. 4F). We confirmed the ciliary structures by co-labeling AcTub and Vasa with ciliary markers. γTub (Fig 4G), Arl13b (Fig. 4H), GluTub (Fig. 4I), and Adcy3 (Fig. 4J), all confirmed AcTub-positive ciliary structures adjacent to negatively stained AcTub-positive CBs. Co-labeling for Vasa, Sycp3, and GluTub further confirmed that the cilia form in prophase oocytes, and similar to zebrafish, within the germline cyst (Fig. 4K, Supp. Fig. 10D). These results show that the zygotene cilium is conserved between sexes and from zebrafish to mouse, and is very likely to be an inherent and fundamental part of the meiosis program.

Discussion

In summary, our work uncovers the novel concept of a cilium as a newly identified player in meiosis that regulates chromosomal pairing and reinforces germ cell morphogenesis. To our knowledge, ciliary involvement in meiosis has not been previously reported in any system.

The bouquet configuration facilitates the mechanics of chromosomal homology searches and pairing and was first described in 1900[11], but fundamental principles of its activity and regulation are still being uncovered. The proteins that tether the telomeric Shelterin complex to Sun proteins on the inner NE were only recently discovered in animals[6,7], and their functional characterization are under pioneering investigation[70,76-78]. Our work now describes the complete framework of the cytoplasmic bouquet machinery, as a cable system assembled by the zygotene cilium, centrosome and microtubules.

We can hypothesize several non-mutually exclusive functions for the zygotene cilium as part of this cable system. First, the cilium could function to anchor the centrosome in order to counter-balance MT movements and telomere rotations. Indeed, our data reveal that the

centrosome at the ciliary base remains fixed in its cellular position, as also shown in mice[9]. In a more active mechanism, the cilium could generate dynein/kinesin motor-dependent forces similar to motile cilia[79,80], that could potentially contribute to bouquet MT movements[81] and telomere rotations. Finally, the zygotene cilia extend throughout the germline cyst and could function through signaling[82-84] to regulate synchronized oocyte development and bouquet execution in the cyst. Ciliary extensions through the cyst could further function mechanically to reinforce this cellular organization. Future experiments will determine the precise mechanisms of function of the zygotene cilium.

Our findings shed new light on reproduction phenotypes in ciliopathies, which so far have been explained by sperm flagella defects and defected motile cilia lining the fallopian tubes and efferent ducts [85,86]. Our study reveals ciliary functions in early differentiating gametes and in fetal ovaries. Severe pediatric ciliopathic syndromes are lethal or lead to severe developmental defects in young children prior to puberty[39-42,87-91], likely masking reproduction phenotypes. In patients with milder ciliopathies, phenotypes could be variable. In our analyses, truncated cilia produced milder phenotypes than their complete loss. Further, *cep290*, *cc2d2a*, and *armc9* females had deficient fertility, but some were able to produce fertilizable eggs. This is in line with reported pleiotropic and variable ciliopathy phenotypes in humans[39-42,87,88]. Thus, our findings propose a previously unrecognized mechanism that potentially additionally contributes to reproduction phenotypes in ciliopathies.

Finally, our work offers the unexpected paradigm that ciliary structures can control nuclear chromosomal dynamics. Most cells in metazoans are ciliated and many exhibit cell type-specific nuclear and/or chromosomal dynamics. We propose that this ciliary regulation of nuclear events may be widely conserved.

Methods

Fish lines and gonad collections

Juvenile ovaries were collected from 5-7 week post-fertilization (wpf) juvenile fish: TU wild type, *cep290*^{fh297} [36], *kif7*^{i271} [43], *cc2d2a*^{w38} [47], *Tg(β–act:Arl13b-GFP)*[92], *Tg(h2a:H2A-GFP)*[93], *Tg(β–act:Cetn2-GFP*[94], *Tg(β–act:Cep55-mCherry)*[95]. Fish had a standard length (SL) measured according to[96], and were consistently ~10-15 mm. Ovary collection was done as in[10,21]. Briefly, to fix the ovaries for immunostaining, and DNA-FISH, fish were cut along the ventral midline and the lateral body wall was removed. The head and tail were removed and the trunk pieces, with the exposed abdomen containing the ovaries, were fixed in 4% PFA at 4°C overnight with nutation. Trunks were then washed in PBS and ovaries were finely dissected in cold PBS. Ovaries were washed in PBS and then either stored in PBS at 4°C in the dark, or dehydrated and stored in 100% MeOH at -20°C in the dark. Testes were collected similarly from 7 wpf juvenile fish and from adult fish and processes similarly. Adult ovaries were collected form wt and mutant fish using similar microdissection and were imaged using a Leica S9i stereomicroscope and camera. Other fish lines analyzed for fertility included *armc9*^{zh505} [51] and *cep290*^{fh378} (unpublished mutant, generated by TALEN-mutagenesis; harbors a 2bp deletion in exon 6).

Fluorescence immunohistochemistry (IHC), and DNA-Telo-FISH

IHC was performed as in[10,21]. Briefly, ovaries were washed 2 times for 5 minutes (2x5min) in PBT (0.3% Triton X-100 in 1xPBS; if stored in MeOH, ovaries were gradually rehydrated first), then washed 4x20min in PBT. Ovaries were blocked for 1.5-2 hours (hr) in blocking solution (10% FBS in PBT) at room temperature, and then incubated with primary antibodies in blocking solution at 4°C overnight. Ovaries were washed 4x20min in PBT and incubated with secondary antibodies in fresh blocking solution for 1.75 hr, and were light protected from this step onward. Ovaries were

washed 4x20min in PBT and then incubated in PBT containing DAPI (1:1000, Molecular Probes), with or without DiOC6 (1:5000, Molecular Probes) for 50 min and washed 2x5min in PBT and 2x5min in PBS. All steps were carried out with nutation. Ovaries were transferred into Vectashield (with DAPI, Vector labs). Ovaries were finally mounted between two #1.5 coverslips using a 120 µm spacer (Molecular Probes).

Primary antibodies used were γTubulin (1:400, Sigma-Aldrich), GFP (1:400; Molecular Probes), Vasa (1:5000)[97], Acetylated tubulin (1:200; Sigma-Aldrich), β-Catenin (1:1000; Sigma-Aldrich), Arl13b[98], glutamylated tubulin (1:400; Adipogen), Sycp3 (1:300, Abcam), γH2Ax (1:400,GeneTex). Secondary antibodies were used at 1:500 (Alexa-flour, Molecular Probes).

DNA-FISH for telomeric repeats (Telo-FISH) was performed using the PNA technique (PNA-Bio) following the company protocol. Hybridization buffer was 70% Formamide, 1 mM Tris pH 7.2, 8.5% MgCl2 buffer (25 mM magnesium chloride, 9 mM citric acid, 82 mM sodium hydrogen phosphate, pH7), 1x Blocking reagent in Maleic acid buffer (100 mM Maleic acid, pH7.5), 0.1% Tween20, 88 nM probe (*5'-CCCTAACCCTAACCCTAA-3',* Cy3- conjugated).

For a combination of IHC with Telo-FISH, IHC was performed first. At the end of the IHC procedure, ovaries were washed an extra time for 30 min in PBT and fixed quickly in 4% PFA for 15-20 min at room temperature. After staining was complete, DAPI (+/- DiOC6) staining and mounting was performed as described above.

Confocal microscopy, image acquisition and processing

Images were acquired on a Zeiss LSM 880 confocal microscope using a 40X lens. The acquisition setting was set between samples and experiments to: XY resolution=1104x1104 pixels, 12-bit, 2x sampling averaging, pixel dwell time=0.59sec, zoom=0.8X, pinhole adjusted to 1.1µm of Z thickness, increments between images in stacks were 0.53µm, laser power and gain

were set in an antibody-dependent manner to 7-11% and 400-650, respectively, and below saturation condition. Unless otherwise noted, shown images are partial Sum Z-projection. Acquired images were not manipulated in a non-linear manner, and only contrast/brightness were adjusted. All figures were made using Adobe Photoshop CC 2014.

Confocal live and time-lapse imaging of cultured ovaries

Live imaging was performed as in[21]. Briefly, ovaries were dissected from juvenile fish (5-7wpf, SL~10-15mm) into fresh warm HL-15 media (Hanks solution containing 60% L-15 (no phenol red), Sigma-Aldrich, and 1:100 Glutamax, Invitrogen, warmed to 28ºC). Ovaries were then embedded in 0.5% low-melt agarose in HL-15 on a glass-bottom dish, and covered with warm HL-15. After the agarose polymerized, ovaries were incubated in HL-15 at 28ºC. Time-lapse images of live ovaries were acquired using either a Zeiss LSM 880 or Nikon Ti2E spinning disc confocal microscopes, both equipped with an environmental chamber set to 28ºC, and using a 40X and 60X lenses, respectively. Images were acquired every 6 seconds for single Z section, or 18-20 seconds for Z stacks, over 5-10 minutes.

Chromosome rotation tracking in live time-lapse images

Live time-lapse imaging of *Tg(h2a:h2a-gfp)* cultured ovaries were performed as above, recording large frames of ovaries, that included multiple zygotene oocytes, oogonia, and somatic pre-granulosa cells side by side, and under identical conditions. Chromosomal dynamics in these cells were tracked based on H2A-GFP intensities, using the TrackMate plugin on ImageJ with the following setting parameters: Blob Diameter was set to 3 microns with an appropriate threshold, and Linking distance was set to 4 microns with maximum permissibility of 2 frame gap for Gap-closing and Gap-closing maximum distance of 1 micron. Identified tracks were confirmed manually. Selected tracks were identified over 20-30 consecutive time points and at least 6.

consecutive time points were selected, and images with at least 2 appropriately identified tracks were analysed. For track visualization, spot sizes were set to 0.21, Tracks were set to show tracks backward, and were color-coded. Tracks were then recorded as an overlay on the original image using the "Capture Overlay" function. For calculating the track % of nuclear perimeter, perimeters of analysed nuclei were measured using ImageJ. Track parameters, including velocity, displacement, and track duration were exported to Excel and GraphPad Prism for statistical analysis.

Coloc2 analysis

A pixel-wise quantitative test for colocalization of AcTub with Arl13b and with GluTub signals was performed using the Coloc 2 plug-in on Fiji as in[10]. Cilia regions of interest (ROI) were taken along individual cilia from representative images. The shape of the ROI varies according to the cilia orientation: ROI of straight cilia are narrower, while ROI of bent or curled cilia are wider, however the spaces taken around the cilia were consistent in all ROI. We calculated a point spread function (PF) of ~1.6 pixels on average for each channel and image, based on PSF= [0.8xExitation wavelength (nm)/objective's NA]/pixel size (nm). Min and max thresholds were automatically set by the plug-in for each image. Pearson correlation coefficient (R) was calculated. R values represent: $-1<R<0$, anti-correlation; $R=0$, no correlation; $0<R<1$, correlation. The plug-in then scrambles the pixels to generate a random image and test for the probability to yield the same Pearson coefficient from a random image. Scrambling was set to 100 iterations, generating 100 different random images from the tested image's pixels. The probability of receiving the calculated Pearson coefficient values for both AcTub and Arl13b and AcTub and gluTub were $p=1$. A pixel-wise quantitative test for colocalization of GluTub with Cep55 was performed similarly.

Image 3D reconstructions in IMARIS

ROIs of whole cysts were extracted from confocal raw data and used to reconstruct nuclei, cilia and other cellular features with respect to each other using blend volume rendering mode. Signal brightness and object transparency were edited in all channels to optimize signal and reduce background. Animation frames were made using the Key Frame Animation Tool.

Serial Block Face Scanning Electron Microscopy (SBF-SEM)

Resin embedded ovaries were mounted onto a cryo pins using conductive silver epoxy and targeted trimming was performed using an ultra-microtome (leica, Milton Keynes, UK) to expose specific area of he ovaries. The trimmed block was painted with Electrodag silver paint and coated with 10 nm AuPd using a Q150T sputter coater (Quorum Technologies).

Cysts were imaged using a Gatan 3View (Gatan, Pleasanton, USA) mounted on a Quanta 250 SEM (FEI, Hillsboro, Oregon, USA). Two areas containing cysts were imaged using the multiple regions of interest (ROI) function, ROI-00, ROI-01. Imaging conditions were as follows; ROI 00, magnification 3445x, pixel size 5.9 nm in x and y, 75nm in z, image dimensions 8189 × 5932 pixels. ROI 01, magnification 3480x, pixel size 5.9 nm in x and y, 75nm in z, frame width 8192 × 5932. Chamber pressure of 70 Pa. 2.8kV, dwell time per pixel 68μs for both RIO's. Before converting the images into Tiff format with Digital Micrograph, they were binned by two giving a final pixel size in x and y of 12nm.

3-D rendering of SBF-SEM images

Renders were made from over 330 75nm sections for each cyst (Supp. Video 4). The image sequence generated from the Serial Block Facing Scanning Electron Microscope (SBF-SEM) was imported into ImageJ. The imported image was then adjusted with the correct voxel

size, brightness, contrast, and alignment. The stack was imported into TrakEM2 canvas for segmentation. In TrakEM2, a project tree was made by adding area lists. Once the Area list was made cell were manually segmented at every 7th to 8th slice using the brush tool of ImageJ and the gap is filled by using the “Interpolation function” of TrakEM2. The segmented structure of the cyst was then exported as “TIFF” file to IMARIS software, and Image properties were set to the acquisition voxel size. Surfaces were created using the surface creation wizard and colour and transparency were set for individual cells. The segmented cells were then exported as “Scenes”. This pipeline was repeated for different structures of the cyst and exported as different scenes from the Area lists. Then the SBF-SEM image stack was imported to the “Arena” area of IMARIS. The voxel size was corrected, and Scenes were imported. Once all the scenes were imported, colour and transparency were set for individual elements for optimal representation. The reconstruction was finally saved using the “Animation” function of IMARIS (Supp. Video 4-5).

Measurements of cilia and CBs in SBF-SEM data

The image sequence was imported as a stack in Fiji. The Image voxel size was set as per the acquisition metadata by selecting image properties. Slices where cytoplasmic bridge or cilia were widest were selected. Using the line tool from the Fiji Menu bar, measuring lines were drawn across the width of the cilia or CBs. The lines drawn were color-coded Red from overlay properties and added to the ROI manager. Three measurement lines were drawn across cilia and CBs longitudinal sections. Two perpendicular lines were drawn across cilia cross sections (along perpendicular diameters). All lines in ROI manager were measured and the result table is saved as a CSV file, and exported to Excel for calculating average width of Cytoplasmic Bridge and Cilia and graphical representation is produced using Graphpad Prism 8.

Measurements of cilia length in confocal data and defining ciliary length categories in wt and mutant ovaries

10 representative cyst ROIs from each genotype were cropped in FIJI and used for image processing in the IMARIS 3D software. The filaments IMARIS feature was used to mark the cilia pathways, as follows. To create the cilium filament, the "Auto-depth" semi-automatic IMARIS algorithm was used, combining user's manual tracking and local signal intensity (Supp. Fig. 5). After creating filaments for all cilia in a cyst, the filament lengths were extracted to EXCEL and GraphPad Prism for statistical analysis, and the images of cilia tracks were extracted as JPEG (Supp. Fig. 5).

We first measured ciliary lengths in wt cysts in 3D as described above and defined ciliary length categories. Wt cilia mostly ranged between 4-8.5 μm, with the longest cilia reaching 12 μm (Fig. 2B). We defined ciliary lengths at 4-8.5 μm as “normal cilia”, and cilia with outlier values <4 μm as “short cilia”. Individual cilia were measured as described above in cysts from all genotypes (Fig. 2B), and the average ciliary length per cyst was calculated (Fig. 2C). Cysts with averages >4 μm were scored cysts with “normal cilia”, cysts with averages <4 μm, were scored as cysts with “short cilia” (Fig. 2C). If no cilia were detected and could not be measured (N.D in Fig. 2B-C), cysts were scored as cysts with “absent cilia”. Distribution of scored cysts were plotted (Fig. 2D) and entire ovaries were scored and their distribution for the same categories was plotted (Fig. 2E).

Bouquet analysis

Bouquet stages span oocytes sizes of 10-15 μm in diameter[10,21], and the telomere cluster might spread wider during early bouquet formation (~10 μm), and later deformation (~15 μm)[21]. We focused on oocytes with clear telomere clusters at mid-bouquet stages (11.5-13 μm)[10,21]. We

co-labeled telomeres by Telo-FISH and the cytoplasm with DiOC6 (Fig. 3C). We scored all oocytes blind to the Telo-FISH channel, and selected oocytes at mid-bouquet sizes (11.5-13 μm), as measured based on the DiOC6 cytoplasmic labeling[21]. We then used the Telo-FISH channel to analyze the distribution of telomeres in the all Z sections spanning these entire oocytes. Categories were defined as "Tight" for telomere clusters at one ole of the nucleus, "Expanded" for wider clusters that spread up to the nuclear equator, and "Dispersed" for unclustered telomeres that spread over the nuclear equator as shown in Fig. 3C.

Quantitative analysis of cyst morphology and integrity

We defined phenotype categories for germline cyst morphology, as follows. "loose cysts" category showed abnormal gaps between sister oocytes in cysts (Fig. 3D). "disintegrated cysts" category phenotype was more severe, showing larger abnormal gaps between cyst oocytes (Fig. 3D), and clear elongated cytoplasmic bridges extending between distant oocytes (Fig. 3D). Normally, at later stages when oocytes leave the cyst, their CBs are detected by MT labeling and appear elongated as they disjoin from their sister oocytes[10]. Within normal cysts, CBs are very challenging to detect by either MT[10] or cytoplasmic labeling without a specific marker (Fig. 3D). This is likely because the cytoplasmic membranes of oocytes interface tightly, masking the fine and short structure of CBs (Supp. Fig. 2). In "disintegrated cysts" the elongated CBs are visible without labeling of MT or specific markers, and are similar to the MT-detected CBs of oocytes that naturally leave the cyst later. They likely represent CBs of oocytes that are separating apart (Fig. 3D).

For quantitative analysis of category phenotypes, and because borders between tight cells in wt cysts are difficult to detect, we measured the distances between the centers of all the neighboring nuclei in 3D in wt, *cep290*$^{-/-}$, and *cep290*$^{-/-}$; *kif7*$^{+/-}$ cysts (Fig. 3E, Supp. Video 7). All distances were normalized to the average oocyte diameter per cyst (Fig. 3E, right panel). 5-8

representative cysts ROIs from each phenotypic category were cropped in FIJI and used for image processing in the IMARIS 3D software. We used semi-automatic segmentation approach to create nuclei surfaces. Each nucleus was segmented in each Z-layer to create a full 3D surface, either by the software automatic segmentation (intensity based) or by marking the nucleus contour manually. After creating surfaces for all cyst nuclei, we used the measurement point feature to calculate the distances between the center of mass of all neighboring nuclei. Distance measurements were exported to an excel sheet and normalized to the average oocyte size (diameter in μm; measured as in[21]) per given cyst. Normalized distances were exported to Graphpad Prism for statistical analysis between groups and generation of dot plots. Images of processed cysts were exported from IMARIS.

Correlation analysis of cyst integrity and ciliary phenotypes

In all cyst morphology experiments we co-labeled cilia by AcTub staining and simultaneously analyzed cyst and cilia phenotypes. To analyze the correlation between cyst and ciliary phenotypes, we pooled gonads from across all examined genotypes and categorized them by the effect on cilia, i.e., normal, short (truncated), or absent (as in Fig. 2), regardless of their genotype. We then asked how many cysts per ciliary phenotypic category were observed in each ovary, and based on this distribution, labeled ovaries as normal, mildly effected, and severely affected (n=43 gonads, 10-60 cysts were analyzed per gonad). We next categorized cyst phenotypes in these ovaries and considered “disintegrated” and “isolated oocytes” categories as severe effects. In most ovaries, a certain cyst phenotype category was predominant in at least 50% of cysts. The ovary category was termed according to this cyst category, or to the most frequently detected one in few cases where no category was frequent in 50% of cysts. The frequency of cyst severity phenotypes were plotted for each ciliary phenotype (Fig. 3I).

Determining stages of spermatogenesis

We identified all spermatogenesis stages in tubules based on their characteristic nuclear morphology and size, using DAPI counter-stain according to[99], as well as the prophase markers telo-FISH, Sycp3 and γH2Ax, as described in the text. Briefly, round spermatids had small round nuclei (2.5 ± 0.1 μm in diameter) and were found towards the center of the tubule as expected. Spermatozoa had compact round nuclei (2.1 ± 0.1 μm in diameter) and were found in the lumen of the tubules as expected. Early round spermatids had a nucleus diameter of 3± 0.1 μm. Round spermatids and spermatozoa were negative to all three prophase markers. Nuclei diameter of Leptotene-Zygotene spermatocytes (L/Z) and pachytene spermatocytes (P) were 5.1+/-0.1 μm and 6+/-0.1 μm, respectively, and both were positive for all prophase markers, showing the expected pattern of each stage[22,56].

Transmission Electron microscopy (TEM)

Gonads were dissected from juvenile fish (5-7 wpf, SL~10-15mm) and fixed as described above in PBS containing 4% PFA and 2.5% glutaraldehyde for overnight at 4°C. Gonads were then rinsed 4 times, 10 minutes each, in 0.1M cacodylate buffer (pH 7.4) and post fixed and stained with 1% osmium tetroxide, 1.5% potassium ferricyanide in 0.1M cacodylate buffer for 1 hour. Ovaries were washed 4 times in cacodylate buffer followed by dehydration in increasing concentrations of ethanol consisting of 30%, 50%, 70%, 80%, 90%, 95%, for 10 minutes each step followed by 100% anhydrous ethanol 3 times, 20 minutes each, and propylene oxide 2 times, 10 minutes each. Following dehydration, the ovaries were infiltrated with increasing concentrations of Agar 100 resin in propylene oxide, consisting of 25, 50, 75, and 100% resin for 16 hours each step. Gonads were embedded in fresh resin and let polymerize in an oven at 60^0C for 48 hours.

Embedded gonads in blocks were sectioned with a diamond knife on a Leica Reichert Ultracut S microtome and ultrathin sections (80nm) were collected onto 200 Mesh, thin bar copper grids. The sections on grids were sequentially stained with Uranyl acetate for 10 minutes and Lead citrate for 10 minutes and imaged with Tecnai 12 TEM 100kV (Phillips) equipped with MegaView II CCD camera and Analysis® version 3.0 software (SoftImaging System GmbH). For TEM images, only the "brightness/contrast" functions on Adobe Photoshop, were mildly adjusted. These adjustments did not affect the biological properties of the imaged cellular features.

In vitro fertilization (IVF)

IVF was performed as in[100]. Briefly, sperm was collected from anesthetized heterozygous or wt males into Hank's solution and stored on ice until eggs are collected. Sperm from two males of the same genotype was collected into a single tube and was used to fertilize eggs collected from control wt, or *cep290*^{fh297}*, or cep290*^{fh378}, or *cc2d2a*^{w38}, or *armc9*^{zh505} homozygous females. Anesthetized wt or mutant females were placed in a dish and squeezed for egg collection. 100-150ul sperm solution was added to the collected eggs, and incubated for 20 seconds. 1ml of E3 containing 0.5% fructose was added to activate sperm, gently mixed and incubated for 2 minutes. 2 ml of E3 was added followed by 5 minutes incubation. The dish was then flooded with E3 and placed in a 28C incubator until examination of fertilization rates.

Mouse ovaries and IHC

Ovaries from fetal mice at day E14.5 were first fixed in trunk with 4% paraformaldehyde in PBS at room temperature for 2 hours, before dissected out and washed briefly in PBS. The ovaries were further permeabilized with 0.3% TritonX-100 in PBS for 30 min at room temperature, followed by blocking with 3% BSA in 0.3% TritonX-100 in PBS for 1 hour at room temperature. Primary antibodies incubation was performed at 4 ℃ for overnight. After 6x20 min washing with

0.3% TritonX-100 in PBS, the ovaries were incubated with secondary antibodies at room temperature for 3 hours. The stained ovaries were finally washed 6x20 min with 0.3% TritonX-100 in PBS, and mounted in 70% glycerol.

Primary antibodies used to stain mice ovaries included: AcTub (1:500, Sigma-Aldrich), Vasa (1:500, R&D systems), gTub (1:500, Adipogen), Arl13b (1:500, Proteintech), Adcy3 (1:500, LSBio). Alexa-flour fluorescent secondary antibodies (Invitrogen) were used at 1:500.

Statistical analysis

All statistical analysis and data plotting was performed using the GraphPad Prism 7 software. Data sets were tested with two-tailed unpaired *t*-test. *p*-values were: *<0.05, **<0.01,****<0.0001, ns=not significant (>0.05).

Acknowledgments

We thank M.C. Mullins, C. Moens, P. Ingham, S. Farber, Z. Sun, B. Perkins, and N. Elia for generously sharing fish lines, and Z. Sun for the zebrafish Arl13b antibody. We thank Y. Buganim for his help with our mouse ovary work. TEM analysis was performed with the help of Y. Friedmann, The Bio-Imaging Unit, at The Alexander Silberman Institute of Life Science of The Hebrew University of Jerusalem. The SBF-SEM analysis was performed with the help of A. Beckett, Biomedical EM Unit, at The University of Liverpool.

This research (grant No. 3291/19) was supported by the ISF Israel-NRF Singapore joint research program to YME and SR, as well as by the Ben Schender Fund for Outstanding Young Scientist to YME, and Dr. Gabrielle Reem-Kayden Scholarship to AM, and KL.

References

1 Chikashige, Y. *et al.* Meiotic proteins bqt1 and bqt2 tether telomeres to form the bouquet arrangement of chromosomes. *Cell* **125**, 59-69, doi:10.1016/j.cell.2006.01.048 (2006).

2 Ding, X. *et al.* SUN1 is required for telomere attachment to nuclear envelope and gametogenesis in mice. *Developmental cell* **12**, 863-872, doi:10.1016/j.devcel.2007.03.018 (2007).

3 Horn, H. F. *et al.* A mammalian KASH domain protein coupling meiotic chromosomes to the cytoskeleton. *The Journal of cell biology* **202**, 1023-1039, doi:10.1083/jcb.201304004 (2013).

4 Morimoto, A. *et al.* A conserved KASH domain protein associates with telomeres, SUN1, and dynactin during mammalian meiosis. *The Journal of cell biology* **198**, 165-172, doi:10.1083/jcb.201204085 (2012).

5 Sato, A. *et al.* Cytoskeletal forces span the nuclear envelope to coordinate meiotic chromosome pairing and synapsis. *Cell* **139**, 907-919, doi:10.1016/j.cell.2009.10.039 (2009).

6 Shibuya, H. *et al.* MAJIN Links Telomeric DNA to the Nuclear Membrane by Exchanging Telomere Cap. *Cell* **163**, 1252-1266, doi:10.1016/j.cell.2015.10.030 (2015).

7 Shibuya, H., Ishiguro, K. & Watanabe, Y. The TRF1-binding protein TERB1 promotes chromosome movement and telomere rigidity in meiosis. *Nature cell biology* **16**, 145-156, doi:10.1038/ncb2896 (2014).

8 Trelles-Sticken, E., Dresser, M. E. & Scherthan, H. Meiotic telomere protein Ndj1p is required for meiosis-specific telomere distribution, bouquet formation and efficient homologue pairing. *The Journal of cell biology* **151**, 95-106 (2000).

9 Shibuya, H., Morimoto, A. & Watanabe, Y. The dissection of meiotic chromosome movement in mice using an in vivo electroporation technique. *PLoS genetics* **10**, e1004821, doi:10.1371/journal.pgen.1004821 (2014).

10 Elkouby, Y. M., Jamieson-Lucy, A. & Mullins, M. C. Oocyte Polarization Is Coupled to the Chromosomal Bouquet, a Conserved Polarized Nuclear Configuration in Meiosis. *PLoS Biol* **14**, e1002335, doi:10.1371/journal.pbio.1002335 (2016).

11 Scherthan, H. A bouquet makes ends meet. *Nature reviews. Molecular cell biology* **2**, 621-627, doi:10.1038/35085086 (2001).

12 Blokhina, Y. P., Nguyen, A. D., Draper, B. W. & Burgess, S. M. The telomere bouquet is a hub where meiotic double-strand breaks, synapsis, and stable homolog juxtaposition are coordinated in the zebrafish, Danio rerio. *PLoS genetics* **15**, e1007730, doi:10.1371/journal.pgen.1007730 (2019).

13 Collins, K. A. *et al.* Corolla is a novel protein that contributes to the architecture of the synaptonemal complex of Drosophila. *Genetics* **198**, 219-228, doi:10.1534/genetics.114.165290 (2014).

14 Fraune, J., Schramm, S., Alsheimer, M. & Benavente, R. The mammalian synaptonemal complex: protein components, assembly and role in meiotic recombination. *Exp Cell Res* **318**, 1340-1346, doi:10.1016/j.yexcr.2012.02.018 (2012).

15 Kohler, S., Wojcik, M., Xu, K. & Dernburg, A. F. Superresolution microscopy reveals the three-dimensional organization of meiotic chromosome axes in intact Caenorhabditis elegans tissue. *Proceedings of the National Academy of Sciences of the United States of America* **114**, E4734-E4743, doi:10.1073/pnas.1702312114 (2017).

16 Lake, C. M. *et al.* Vilya, a component of the recombination nodule, is required for meiotic double-strand break formation in Drosophila. *eLife* **4**, e08287, doi:10.7554/eLife.08287 (2015).

17 Rog, O., Kohler, S. & Dernburg, A. F. The synaptonemal complex has liquid crystalline properties and spatially regulates meiotic recombination factors. *eLife* **6**, doi:10.7554/eLife.21455 (2017).

18 Schucker, K., Holm, T., Franke, C., Sauer, M. & Benavente, R. Elucidation of synaptonemal complex organization by super-resolution imaging with isotropic resolution. *Proceedings of the National Academy of Sciences of the United States of America* **112**, 2029-2033, doi:10.1073/pnas.1414814112 (2015).

19 Cahoon, C. K. & Hawley, R. S. Regulating the construction and demolition of the synaptonemal complex. *Nat Struct Mol Biol* **23**, 369-377, doi:10.1038/nsmb.3208 (2016).

20 Gyuricza, Mercedes R. *et al.* Dynamic and Stable Cohesins Regulate Synaptonemal Complex Assembly and Chromosome Segregation. *Current Biology* **26**, 1688-1698, doi:https://doi.org/10.1016/j.cub.2016.05.006 (2016).

21 Elkouby, Y. & Mullins, M. Methods for the analysis of early oogenesis in zebrafish. *Developmental biology* **430**, 310-324 (2017).

22 Saito, K., Sakai, C., Kawasaki, T. & Sakai, N. Telomere distribution pattern and synapsis initiation during spermatogenesis in zebrafish. *Developmental dynamics : an official publication of the American Association of Anatomists* **243**, 1448-1456, doi:10.1002/dvdy.24166 (2014).

23 Reiter, J. F., Blacque, O. E. & Leroux, M. R. The base of the cilium: roles for transition fibres and the transition zone in ciliary formation, maintenance and compartmentalization. *EMBO Rep* **13**, 608-618, doi:10.1038/embor.2012.73 (2012).

24 Mirvis, M., Stearns, T. & James Nelson, W. Cilium structure, assembly, and disassembly regulated by the cytoskeleton. *Biochemical Journal* **475**, 2329-2353, doi:10.1042/bcj20170453 (2018).

25 Duldulao, N. A., Lee, S. & Sun, Z. Cilia localization is essential for in vivo functions of the Joubert syndrome protein Arl13b/Scorpion. *Development* **136**, 4033-4042, doi:10.1242/dev.036350 (2009).

26 Higginbotham, H. *et al.* Arl13b-regulated cilia activities are essential for polarized radial glial scaffold formation. *Nat Neurosci* **16**, 1000-1007, doi:10.1038/nn.3451 (2013).

27 Li, J. & Ge, W. Zebrafish as a model for studying ovarian development: Recent advances from targeted gene knockout studies. *Molecular and Cellular Endocrinology* **507**, 110778, doi:https://doi.org/10.1016/j.mce.2020.110778 (2020).

28 Pepling, M. E., de Cuevas, M. & Spradling, A. C. Germline cysts: a conserved phase of germ cell development? *Trends in cell biology* **9**, 257-262 (1999).

29 Lu, K., Jensen, L., Lei, L. & Yamashita, Y. M. Stay Connected: A Germ Cell Strategy. *Trends in Genetics* **33**, 971-978, doi:https://doi.org/10.1016/j.tig.2017.09.001 (2017).

30 Greenbaum, M. P., Ma, L. & Matzuk, M. M. Conversion of midbodies into germ cell intercellular bridges. *Developmental biology* **305**, 389-396, doi:10.1016/j.ydbio.2007.02.025 (2007).

31 Marlow, F. L. & Mullins, M. C. Bucky ball functions in Balbiani body assembly and animal-vegetal polarity in the oocyte and follicle cell layer in zebrafish. *Developmental biology* **321**, 40-50, doi:10.1016/j.ydbio.2008.05.557 (2008).

32 Leu, D. H. & Draper, B. W. The ziwi promoter drives germline-specific gene expression in zebrafish. *Developmental dynamics : an official publication of the American Association of Anatomists* **239**, 2714-2721, doi:10.1002/dvdy.22404 (2010).

33 Ishikawa, T. Axoneme Structure from Motile Cilia. *Cold Spring Harb Perspect Biol* **9**, doi:10.1101/cshperspect.a028076 (2017).

34 Haglund, K., Nezis, I. P. & Stenmark, H. Structure and functions of stable intercellular bridges formed by incomplete cytokinesis during development. *Commun Integr Biol* **4**, 1-9, doi:10.4161/cib.4.1.13550 (2011).

35 Gershony, O. *et al.* Measuring abscission spatiotemporal dynamics using quantitative high-resolution microscopy. *Methods Cell Biol* **137**, 205-224, doi:10.1016/bs.mcb.2016.03.032 (2017).

36 Lessieur, E. M. *et al.* Ciliary genes arl13b, ahi1 and cc2d2a differentially modify expression of visual acuity phenotypes but do not enhance retinal degeneration due to mutation of cep290 in zebrafish. *PLOS ONE* **14**, e0213960, doi:10.1371/journal.pone.0213960 (2019).

37 Betleja, E. & Cole, D. G. Ciliary Trafficking: CEP290 Guards a Gated Community. *Current Biology* **20**, R928-R931, doi:https://doi.org/10.1016/j.cub.2010.09.058 (2010).

38 Li, C. *et al.* MKS5 and CEP290 Dependent Assembly Pathway of the Ciliary Transition Zone. *PLoS Biol* **14**, e1002416, doi:10.1371/journal.pbio.1002416 (2016).

39 Baala, L. *et al.* Pleiotropic effects of CEP290 (NPHP6) mutations extend to Meckel syndrome. *Am J Hum Genet* **81**, 170-179, doi:10.1086/519494 (2007).

40 Coppieters, F., Lefever, S., Leroy, B. P. & De Baere, E. CEP290, a gene with many faces: mutation overview and presentation of CEP290base. *Hum Mutat* **31**, 1097-1108, doi:10.1002/humu.21337 (2010).

41 Frank, V. *et al.* Mutations of the CEP290 gene encoding a centrosomal protein cause Meckel-Gruber syndrome. *Hum Mutat* **29**, 45-52, doi:10.1002/humu.20614 (2008).

42 Valente, E. M. *et al.* Mutations in CEP290, which encodes a centrosomal protein, cause pleiotropic forms of Joubert syndrome. *Nat Genet* **38**, 623-625, doi:10.1038/ng1805 (2006).

43 Maurya, A. K. *et al.* Positive and negative regulation of Gli activity by Kif7 in the zebrafish embryo. *PLoS genetics* **9**, e1003955, doi:10.1371/journal.pgen.1003955 (2013).

44 Barakeh, D. *et al.* The many faces of KIF7. *Hum Genome Var* **2**, 15006, doi:10.1038/hgv.2015.6 (2015).

45 He, M. *et al.* The kinesin-4 protein Kif7 regulates mammalian Hedgehog signalling by organizing the cilium tip compartment. *Nature cell biology* **16**, 663-672, doi:10.1038/ncb2988 (2014).

46 Putoux, A. *et al.* KIF7 mutations cause fetal hydrolethalus and acrocallosal syndromes. *Nature Genetics* **43**, 601, doi:10.1038/ng.826

https://www.nature.com/articles/ng.826#supplementary-information (2011).

47 Bachmann-Gagescu, R. *et al.* The ciliopathy gene cc2d2a controls zebrafish photoreceptor outer segment development through a role in Rab8-dependent vesicle trafficking. *Human Molecular Genetics* **20**, 4041-4055, doi:10.1093/hmg/ddr332 (2011).

48 Garcia-Gonzalo, F. R. *et al.* A transition zone complex regulates mammalian ciliogenesis and ciliary membrane composition. *Nature Genetics* **43**, 776-784, doi:10.1038/ng.891 (2011).

49 Breslow, D. K. *et al.* A CRISPR-based screen for Hedgehog signaling provides insights into ciliary function and ciliopathies. *Nature Genetics* **50**, 460-471, doi:10.1038/s41588-018-0054-7 (2018).

50 Latour, B. L. *et al.* Dysfunction of the ciliary ARMC9/TOGARAM1 protein module causes Joubert syndrome. *The Journal of Clinical Investigation* **130**, 4423-4439, doi:10.1172/JCI131656 (2020).

51 Van De Weghe, J. C. *et al.* Mutations in ARMC9, which Encodes a Basal Body Protein, Cause Joubert Syndrome in Humans and Ciliopathy Phenotypes in Zebrafish. *The American Journal of Human Genetics* **101**, 23-36, doi:https://doi.org/10.1016/j.ajhg.2017.05.010 (2017).

52 Dranow, D. B., Tucker, R. P. & Draper, B. W. Germ cells are required to maintain a stable sexual phenotype in adult zebrafish. *Developmental biology* **376**, 43-50, doi:10.1016/j.ydbio.2013.01.016 (2013).

53 Rodriguez-Mari, A. *et al.* Sex reversal in zebrafish fancl mutants is caused by Tp53-mediated germ cell apoptosis. *PLoS genetics* **6**, e1001034, doi:10.1371/journal.pgen.1001034 (2010).

54 Anderson, J. L. *et al.* Multiple sex-associated regions and a putative sex chromosome in zebrafish revealed by RAD mapping and population genomics. *PLoS One* **7**, e40701, doi:10.1371/journal.pone.0040701 (2012).

55 Maack, G. & Segner, H. Morphological development of the gonads in zebrafish. *J Fish Biol* **62**, 895-906, doi:Doi 10.1046/J.1095-8649.2003.00074.X (2003).

56 Saito, K., Siegfried, K. R., Nusslein-Volhard, C. & Sakai, N. Isolation and cytogenetic characterization of zebrafish meiotic prophase I mutants. *Developmental dynamics : an official publication of the American Association of Anatomists* **240**, 1779-1792, doi:10.1002/dvdy.22661 (2011).

57 Bolcun-Filas, E., Rinaldi, V. D., White, M. E. & Schimenti, J. C. Reversal of female infertility by Chk2 ablation reveals the oocyte DNA damage checkpoint pathway. *Science* **343**, 533-536, doi:10.1126/science.1247671 (2014).

58 Di Giacomo, M. *et al.* Distinct DNA-damage-dependent and -independent responses drive the loss of oocytes in recombination-defective mouse mutants. *Proceedings of the National Academy of Sciences of the United States of America* **102**, 737-742, doi:10.1073/pnas.0406212102 (2005).

59 Leerberg, D. M., Sano, K. & Draper, B. W. Fibroblast growth factor signaling is required for early somatic gonad development in zebrafish. *PLoS genetics* **13**, e1006993, doi:10.1371/journal.pgen.1006993 (2017).

60 Andersen, J. S. *et al.* Proteomic characterization of the human centrosome by protein correlation profiling. *Nature* **426**, 570-574, doi:10.1038/nature02166 (2003).

61 Chang, B. *et al.* In-frame deletion in a novel centrosomal/ciliary protein CEP290/NPHP6 perturbs its interaction with RPGR and results in early-onset retinal degeneration in the rd16 mouse. *Human Molecular Genetics* **15**, 1847-1857, doi:10.1093/hmg/ddl107 (2006).

62 Sayer, J. A. *et al.* The centrosomal protein nephrocystin-6 is mutated in Joubert syndrome and activates transcription factor ATF4. *Nat Genet* **38**, 674-681, doi:10.1038/ng1786 (2006).

63 Tsang, W. Y. *et al.* CP110 Suppresses Primary Cilia Formation through Its Interaction with CEP290, a Protein Deficient in Human Ciliary Disease. *Developmental cell* **15**, 187-197, doi:https://doi.org/10.1016/j.devcel.2008.07.004 (2008).

64 Stowe, T. R., Wilkinson, C. J., Iqbal, A. & Stearns, T. The centriolar satellite proteins Cep72 and Cep290 interact and are required for recruitment of BBS proteins to the cilium. *Molecular biology of the cell* **23**, 3322-3335, doi:10.1091/mbc.e12-02-0134 (2012).

65 Fu, J., Hagan, I. M. & Glover, D. M. The centrosome and its duplication cycle. *Cold Spring Harb Perspect Biol* **7**, a015800, doi:10.1101/cshperspect.a015800 (2015).

66 Nigg, E. A. & Stearns, T. The centrosome cycle: Centriole biogenesis, duplication and inherent asymmetries. *Nature cell biology* **13**, 1154-1160, doi:10.1038/ncb2345 (2011).

67 Lehti, M. S. & Sironen, A. Formation and function of sperm tail structures in association with sperm motility defects†. *Biology of reproduction* **97**, 522-536, doi:10.1093/biolre/iox096 (2017).

68 Penkner, A. M. *et al.* Meiotic chromosome homology search involves modifications of the nuclear envelope protein Matefin/SUN-1. *Cell* **139**, 920-933, doi:10.1016/j.cell.2009.10.045 (2009).

69 Conrad, M. N., Dominguez, A. M. & Dresser, M. E. Ndj1p, a meiotic telomere protein required for normal chromosome synapsis and segregation in yeast. *Science* **276**, 1252-1255 (1997).

70 Long, J. *et al.* Telomeric TERB1-TRF1 interaction is crucial for male meiosis. *Nat Struct Mol Biol*, doi:10.1038/nsmb.3496 (2017).

71 Pendlebury, D. F. *et al.* Dissecting the telomere-inner nuclear membrane interface formed in meiosis. *Nat Struct Mol Biol*, doi:10.1038/nsmb.3493 (2017).

72 Arora, R. *et al.* Meiotic onset is reliant on spatial distribution but independent of germ cell number in the mouse ovary. *Journal of Cell Science* **129**, 2493-2499, doi:10.1242/jcs.189910 (2016).

73 Miles, D. C., van den Bergen, J. A., Sinclair, A. H. & Western, P. Regulation of the female mouse germ cell cycle during entry into meiosis. *Cell Cycle* **9**, 408-418, doi:10.4161/cc.9.2.10691 (2010).

74 Soh, Y. Q. S. *et al.* Meioc maintains an extended meiotic prophase I in mice. *PLoS genetics* **13**, e1006704, doi:10.1371/journal.pgen.1006704 (2017).

75 Vernet, N. *et al.* Meiosis occurs normally in the fetal ovary of mice lacking all retinoic acid receptors. *Science Advances* **6**, eaaz1139, doi:10.1126/sciadv.aaz1139 (2020).

76 Dunce, J. M. *et al.* Structural basis of meiotic telomere attachment to the nuclear envelope by MAJIN-TERB2-TERB1. *Nature Communications* **9**, 5355, doi:10.1038/s41467-018-07794-7 (2018).

77 Wang, Y. *et al.* The meiotic TERB1-TERB2-MAJIN complex tethers telomeres to the nuclear envelope. *Nature Communications* **10**, 564, doi:10.1038/s41467-019-08437-1 (2019).

78 Zhang, J., Tu, Z., Watanabe, Y. & Shibuya, H. Distinct TERB1 Domains Regulate Different Protein Interactions in Meiotic Telomere Movement. *Cell reports* **21**, 1715-1726, doi:10.1016/j.celrep.2017.10.061 (2017).

79 Khan, S. & Scholey, J. M. Assembly, Functions and Evolution of Archaella, Flagella and Cilia. *Current Biology* **28**, R278-R292, doi:https://doi.org/10.1016/j.cub.2018.01.085 (2018).

80 Mitchison, T. J. & Mitchison, H. M. How cilia beat. *Nature* **463**, 308-309, doi:10.1038/463308a (2010).

81 Lee, C. Y. *et al.* Mechanism and Regulation of Rapid Telomere Prophase Movements in Mouse Meiotic Chromosomes. *Cell reports*, doi:10.1016/j.celrep.2015.03.045 (2015).

82 Gigante, E. D. & Caspary, T. Signaling in the primary cilium through the lens of the Hedgehog pathway. *WIREs Developmental Biology* **9**, e377, doi:10.1002/wdev.377 (2020).

83 Singla, V. & Reiter, J. F. The Primary Cilium as the Cell's Antenna: Signaling at a Sensory Organelle. *Science* **313**, 629-633, doi:10.1126/science.1124534 (2006).

84 Wheway, G., Nazlamova, L. & Hancock, J. T. Signaling through the Primary Cilium. *Frontiers in Cell and Developmental Biology* **6**, doi:10.3389/fcell.2018.00008 (2018).

85 Wallmeier, J. *et al.* Motile ciliopathies. *Nature Reviews Disease Primers* **6**, 77, doi:10.1038/s41572-020-0209-6 (2020).

86 Terre, B. *et al.* Defects in efferent duct multiciliogenesis underlie male infertility in GEMC1-, MCIDAS- or CCNO-deficient mice. *Development* **146**, doi:10.1242/dev.162628 (2019).

87 Zahid, S. *et al.* in *Retinal Dystrophy Gene Atlas* 47-49 (Springer International Publishing, 2018).

88 Moradi, P., Davies, W. L., Mackay, D. S., Cheetham, M. E. & Moore, A. T. Focus on molecules: centrosomal protein 290 (CEP290). *Exp Eye Res* **92**, 316-317, doi:10.1016/j.exer.2010.05.009 (2011).

89 Forsythe, E. & Beales, P. L. Bardet–Biedl syndrome. *European Journal of Human Genetics* **21**, 8-13, doi:10.1038/ejhg.2012.115 (2013).

90 Hartill, V., Szymanska, K., Sharif, S. M., Wheway, G. & Johnson, C. A. Meckel–Gruber Syndrome: An Update on Diagnosis, Clinical Management, and Research Advances. *Frontiers in Pediatrics* **5**, doi:10.3389/fped.2017.00244 (2017).

91 Romani, M., Micalizzi, A. & Valente, E. M. Joubert syndrome: congenital cerebellar ataxia with the molar tooth. *The Lancet Neurology* **12**, 894-905, doi:https://doi.org/10.1016/S1474-4422(13)70136-4 (2013).

92 Borovina, A., Superina, S., Voskas, D. & Ciruna, B. Vangl2 directs the posterior tilting and asymmetric localization of motile primary cilia. *Nature cell biology* **12**, 407-412, doi:10.1038/ncb2042 (2010).

93 Pauls, S., Geldmacher-Voss, B. & Campos-Ortega, J. A. A zebrafish histone variant H2A.F/Z and a transgenic H2A.F/Z:GFP fusion protein for in vivo studies of embryonic development. *Dev Genes Evol* **211**, 603-610, doi:10.1007/s00427-001-0196-x (2001).

94 Novorol, C. *et al.* Microcephaly models in the developing zebrafish retinal neuroepithelium point to an underlying defect in metaphase progression. *Open Biology* **3**, 130065, doi:doi:10.1098/rsob.130065 (2013).

95 Adar-Levor, S. *et al.* Cytokinetic abscission is part of the mid-blastula transition switch in early zebrafish embryogenesis. *bioRxiv*, 2020.2007.2026.221515, doi:10.1101/2020.07.26.221515 (2020).

96 Parichy, D. M., Elizondo, M. R., Mills, M. G., Gordon, T. N. & Engeszer, R. E. Normal table of postembryonic zebrafish development: staging by externally visible anatomy of the living fish.

Developmental dynamics : an official publication of the American Association of Anatomists **238**, 2975-3015, doi:10.1002/dvdy.22113 (2009).

97 Knaut, H., Pelegri, F., Bohmann, K., Schwarz, H. & Nusslein-Volhard, C. Zebrafish vasa RNA but not its protein is a component of the germ plasm and segregates asymmetrically before germline specification. *The Journal of cell biology* **149**, 875-888 (2000).

98 Duldulao, N. A., Lee, S. & Sun, Z. Cilia localization is essential for in vivo functions of the Joubert syndrome protein Arl13b/Scorpion. *Development* **136**, 4033-4042, doi:10.1242/dev.036350 (2009).

99 Leal, M. C. *et al.* Histological and stereological evaluation of zebrafish (Danio rerio) spermatogenesis with an emphasis on spermatogonial generations. *Biology of reproduction* **81**, 177-187, doi:10.1095/biolreprod.109.076299 (2009).

100 Dingare, C. *et al.* The Hippo pathway effector Taz is required for cell morphogenesis and fertilization in zebrafish. *Development* **145**, dev167023, doi:10.1242/dev.167023 (2018).